Hyperspectral Imaging Performance

Mariusz E. Grøtte[1], João Fortuna[1], Julian Veisdal[2], Fred Sigernes[3], Evelyn Honoré-Livermore[4], Tor Arne Johansen[1];

I. HYPERSPECTRAL IMAGER (HSI) PAYLOAD

A. Instrument design

The HSI is designed based on a grating spectrograph (without prism). Fig. 1 shows the layout of an optical diagram which visualizes a center cross section of the instrument perpendicular to the slits, parallel to the axis of refraction.
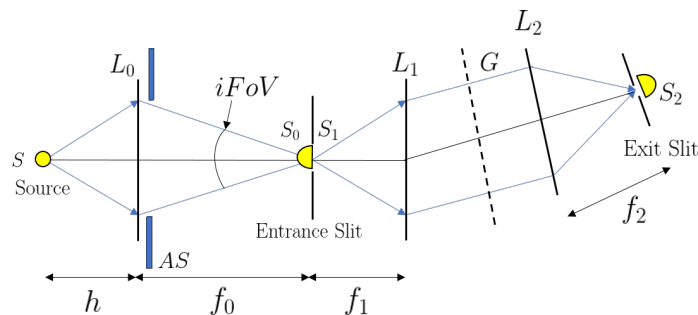

Fig. 1: Optical diagram of Spectrometer. L_0 is the front lens with aperture stop taken to be AS here, f_0 is the focal length between L_0 and entrance slit, S_0 is the field lens, f_1 is the distance between entrance slit S_1 and collimator lens L_1, G is the grating, f_2 is the distance between the grating G and detector lens L_2. Credit: Fred Sigernes.

Amongst several other methods to avoid stray light into the collimator lens, the field lens S_1 is attached to the front (or back) of the entrance slit. The current HSI is depicted in Figure 2, and shows an angle ($\beta = 20°$?) to the diffracted light reaching the sensor. Table I provide the optical dimensions related to Fig. 1 for the current HSI (version 4.1) and proposed space HSI (version 4.2). Further specifications are given in Table II that describe the HSI performance.

Fig. 2: Current HSI version 4. Credit: Fred Sigernes.

[1]Center for Autonomous Marine Operations and Systems (AMOS), Department of Engineering Cybernetics, Norwegian University of Science and Technology, Trondheim, Norway.
[2]MOON Wearables, Trondheim, Norway.
[3]University Center in Svalbard (UNIS), N-9171 Longyearbyen, Norway.
[4]Department of Electronic Systems, Norwegian University of Science and Technology, Trondheim, Norway.

TABLE I: Current HSI version 4-1 Optics Dimensions, HSI version 4-2 changes and version 5 indicated at the bottom

Part	Dimensions	Description
HSI ver. 4-1		
$f_0/\#$	$f_0/4$	f-number front lens
$A_0(L_0)$	4 mm	Aperture front lens
L_0	14 mm	Front lens diameter
f_0	16 mm	Focal length front lens
w	0.025 mm	Entrance slit width
z	3 mm	Entrance slit height
S_1	10 mm	Field lens aperture
$f_1/\#$	$f_1/3.33$	f-number collimator lens
$A_1(L_1)$	9 mm	Aperture collimator lens
f_1	30 mm	Focal length collimator
G	25×25 mm^2	Grating area
$f_2/\#$	$f_2/2.5$	f-number detector lens
$A_2(L_2)$	10 mm	Aperture detector lens
f_2	25 mm	Focal length detector lens
HSI ver. 4-2		
$A_0(L_0)$	12.5 mm	Aperture front lens
f_0	50 mm	Focal length front lens
HSI ver. 5		
$f_0/\#$	$f_0/2.8$	f-number front lens
$A_0(L_0)$	3.714 mm	Aperture front lens
f_0	10.4 mm	Focal length front lens
w	0.075 mm	Aperture front lens

TABLE II: HSI version 4-1 Specifications

Spectral range	400-900 nm
Bandpass $\Delta\lambda$	5 nm
Mass m	152 g
Size $w \times h \times L$	$47 \times 58 \times 130$ mm
$iFoV$	$0.0286° \times 3.4367°$
Sampling	0.342 nm/pixel
Pixel size	5.5 μpixel
Binning	2×2
Grating	600 lines/mm
Usable bands	100
Sensor resolution	2048×1088 pixels
Number of effective pixels N	578 pixels
Optical efficiency η_{OE}	see Figure 7
Quantum efficiency η_{QE}	0.8-0.9
Dark current	125 e^-/s
Read-out noise (25 C°)	13 e^-

B. Nadir-Pointing Performance

Since the satellite will be in a sun-synchronous orbit at $h \approx 500$ km altitude, the FoV may be calculated as follows:

$$iFoV = \tan\frac{w}{f_0} \times \tan\frac{z}{f_0} \tag{1}$$

giving $iFoV = 0.0286° \times 3.4367°$ (Vertical $\times$ Horizontal). This results in larger pixels along the direction of flight as compared to lower altitudes, and defines the spatial resolution as illustrated in Fig 3. The distance δx defines the ground segment optical resolution as seen by the instrument at time $t = t_0$ and is the instantaneous ground resolution. This is expressed as,

$$\delta x = \frac{hw}{f_0} \tag{2}$$

where h is the orbit altitude and δx is connected to spectral bandpass BP through the width of the slit w and raw instantaneous sampling is shown in Fig 4. The spatial resolution may then be calculated as,

$$\Delta x = \delta x + v_{\text{sat}}\Delta t \tag{3}$$

where $\Delta t = t_1 - t_0$ is the exposure time and v_{sat} is the speed of the satellite. It does not include the read-out time τ for the sensor but the criterion for read-out time may be determined as,

$$\tau \le \left(\frac{hw}{f_0 v_{\text{sat}}} \right) \tag{4}$$

Normal to the flight direction the resolution is calculated simply as

$$\Delta y = \frac{hz}{f_0 N_p} \tag{5}$$

where N_p is the effective number of pixels along the slit image.

For the space HSI specs f_0 =50 mm, aperture $f/4$ and $N_p = 580$, this gives δx =250 m, Δx =500 m, δy =51.875 m with exposure time of $\Delta t = 0.0328$ s (read-out time should be less than or equal to this) and 31 frames per second ($1/(\Delta t) \approx 31$ fps). Main characteristics of HSI imaging at Nadir are given in Table III.
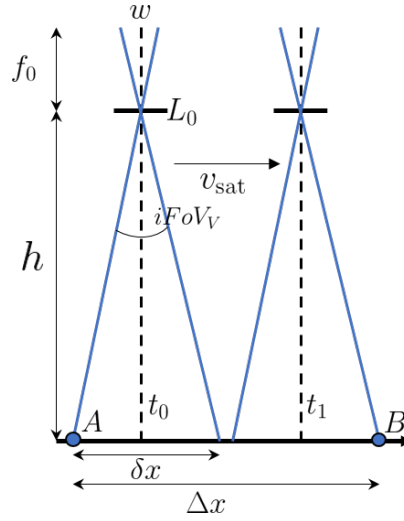

Fig. 3: Field of view of slit as satellite moves with velocity v_{sat}. w is the slit width and $L0$ is front lens with focal length f_0. h is altitude above ground level. The spatial resolution then becomes equal to the distance from point A to B denoted as Δx.
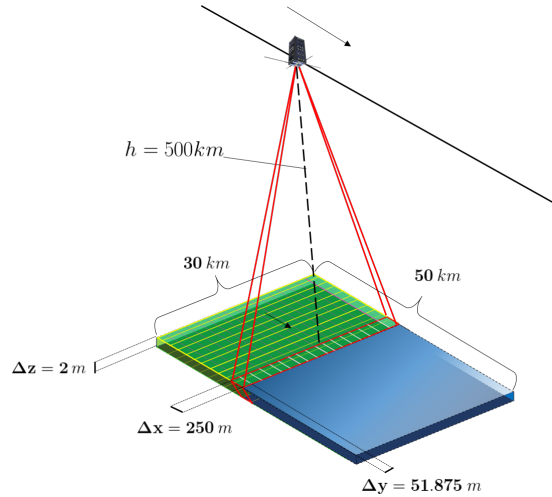

Fig. 4: Overhead optical sampling of 50×30 km target area with optical resolution $\delta x = 250$ m.

TABLE III: HSI version 4-1 characteristics for Nadir-looking sensor $\gamma = 0°$

Altitude h	500 km
N_p	580 pixels
Exposure time Δt	32.8 ms
Swath Width	30 km
δx	250 m
Δx	500 m
Δy	51.875 m
v_{sat}	7.6127 km/s

II. CAMERA SENSITIVITY ANALYSIS

This section covers the sensitivity analysis of optics performance to determine feasibility of the sensor and image acquisition from Low-Earth-Orbit (LEO) at $h = 500$ km.

A. Remote Sensing

The methodology is based on relevant calculations from Ocean Optics Website[1] and a RESONON white paper on SNR[2]. It can be seen in Fig. 5 that significant atmospheric disturbances increases with altitude but not much more over Top of Atmosphere (ToA) as compared to 30 000 m. Radiances in $\text{Wm}^{-2}\text{sr}^{-1}\text{nm}^{-1}$ are modeled with the following MODTRAN inputs as assumptions:

- cloudless mid-latitude summer atmosphere
- marine aerosols present
- relative humidity of 76% at sea level
- solar zenith angle of 50 deg
- surface wind speed of $6m/s$
- Nadir-viewing sensor ($\gamma = 0°$)
- horizontal visibility of $63km$
- homogeneous water
- Case 1 water with Chl-a concentration of $1mg/m^{-3}$
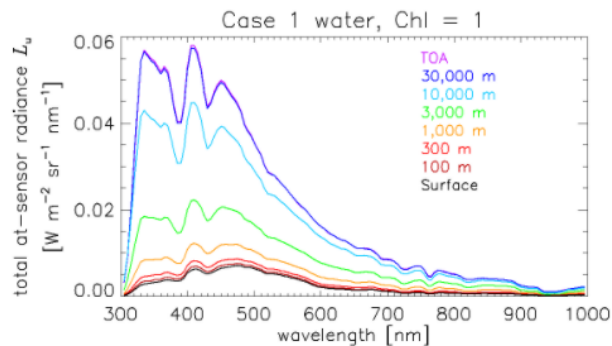- infinitely deep water

Fig. 5: Example generated (from HydroLight software) radiances L_u for different HSI sensor altitudes with Case 1 water and Chl-a concentrations of 1 mg/m^3. The water-leaving radiance and surface-reflected radiance (not shown) are the same in all cases. Shows significant atmospheric disturbances with increasing altitude. Reference: http://www.oceanopticsbook.info

The radiances are re-run in HydroLight software for spectral range of 400-900 nm with spectral resolution of 5 nm in Figure 6.

[1]http://www.oceanopticsbook.info
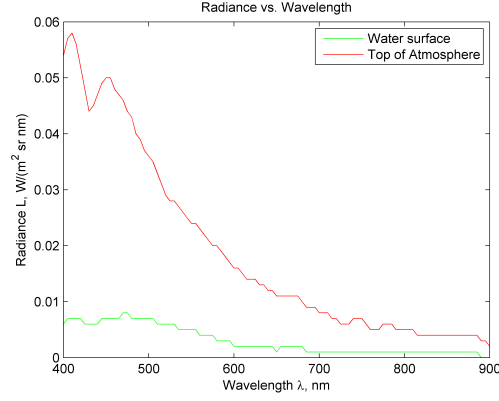[2]https://www.resonon.com

Fig. 6: L_u reaching the HSI sensor in-situ and top of atmosphere (ToA) which determines amount of photons detected at each spectral band with $\Delta\lambda = 5$ nm. Assumed is Case 1 water and Chl-a concentrations of 1 mg/m^3. Reference: http://www.oceanopticsbook.info.

B. Theoretical Signal-to-Noise Ratio (SNR)

One of the indicators to understand the performance of the camera with respect to a desired signal or photons reaching the sensor is to determine the signal-to-noise ratio (SNR). The constants for the HSI are required to determine photon count as shown in Tables II and IV.

TABLE IV: Sensor characteristics for Nadir-looking HSI in SSO

Altitude h	500 km
Viewing angle γ	$0°$
Slant range r	$h/\cos\gamma = 500$ km
δx	250 m
Δy	51.875 m
A_{ground}	$\delta x \times \Delta y = 1.2969 \times 10^4$ m^2
v_{sat}	7.6127 km/s

The sensor and grating efficiencies at each wavelength are shown in Figure 7. The quantum efficiency is assumed to be worst case at 80 % for all wavelengths (although it varies across different λ).
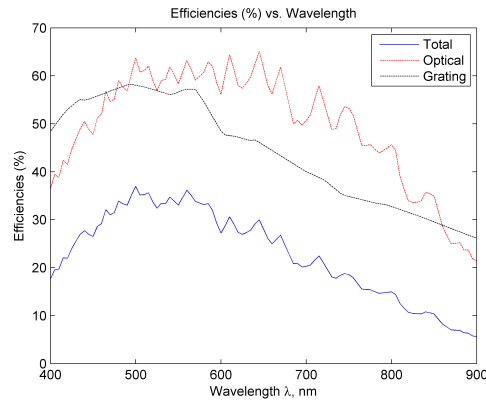

Fig. 7: Efficiencies to be expected for HSI sensor across several wavelengths. Source: CMOSIS CMV2000 NIR-enhanced sensor specifications http://www.cmosis.com.

Assuming viewing angle $\gamma = 0°$, the solid angle of the sensor as seen from the earth's surface is

$$\Omega_{\text{aperture}} = \frac{\pi(L_0/2)^2}{h^2} = 4.9087 \times 10^{-16} sr \tag{6}$$

The power detected by the sensor coming from a square of $A_{\text{ground}} = 1.2969 \times 10^4$ m^2 of the ocean surface is

$$
\begin{aligned}
P_{\text{detector}} &= L\Omega_{\text{aperture}}A_{\text{ground}}\eta_{\text{OE}}\Delta\lambda \\
&= (0.03 Wm^{-2}sr^{-1}nm^{-1}) \times (4.9087 \times 10^{-16}sr) \\
&\quad \times (1.2969 \times 10^4 m^2) \times (0.5) \times (5nm) \\
&\approx 4.7745 \times 10^{-13}W
\end{aligned}
\tag{7}
$$

Where L is the irradiance reaching the fron lens at Top of Atmosphere for $\lambda = 550$ nm. If we assume a selected wavelength of $\lambda = 550$ nm, the corresponding number of photo-electrons released in the detector in time $\Delta t = 0.0328$ seconds is

$$
\begin{aligned}
N_{\text{electrons}} &= P_{\text{detector}}\Delta t\eta_{\text{QE}}\frac{\lambda}{h_{\text{planck}}c} \\
&= (4.7745 \times 10^{-13}Js^{-1}) \times (0.0328s) \times (0.8) \\
&\quad \times \left(\frac{550 \times 10^{-9}nm}{(6.63 \times 10^{-34}Js) \times (3 \times 10^8 ms^{-1})}\right) \\
&\approx 3.0350 \times 10^4
\end{aligned}
\tag{8}
$$

where h_{planck} and c are Planck's constant and speed of light, respectively. The exposure time $\Delta t = 0.0328$ determines how much the satellite sees in a movement of $v_{\text{sat}} \times \Delta t = 250$ m, i.e. spatial resolution of $\Delta x = \delta x + v_{\text{sat}} \times \Delta t = 500$ m at Nadir. The amount of photons collected in one pixel come from an area equivalent to $\delta x \times \Delta y = 1.2969 \times 10^4$ m^2. Of a total of 3.0350×10^4 photon-electrons, 3035 water-leaving photon-electrons reach the sensor due to the atmospheric effects shown in Figure 6 where ≈ 10 % of total photons consists of water-leaving photons. Using the numbers from Table IV, the SNR is calculated as follows,

$$
\begin{aligned}
SNR &= \frac{N_{\text{electrons}}}{\sqrt{N_{\text{electrons}} + B(i_{\text{dark}}) \times \Delta t + B(e_{\text{read}}^2)}} \\
&= \frac{3 \times 10^4}{\sqrt{3 \times 10^4 + 2 \times 125/s \times 0.0328s + 2 \times 13^2}} \\
&\approx 172.42
\end{aligned}
\tag{9}
$$

Where B is number of binning operations. It is assumed that binning operations are 2×2 that are incorporated into achieving spectral resolution of $\Delta\lambda = 5$ nm, although this has little effect on the SNR. Effectively SNR of water-leaving radiance will be $\approx 17:1$

C. Optics

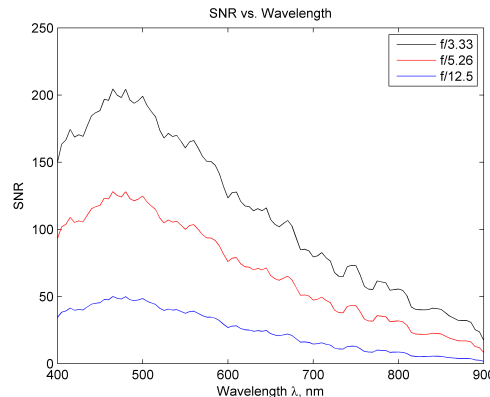Figure 8 shows the sensitivity of SNR to front lens aperture size (A_0)

Fig. 8: SNR vs. aperture, clearly showing increase in SNR as aperture of lens increases.

D. Exposure Time

Figure 9 shows the sensitivity of SNR to exposure time Δt. The main compromise here will be between spatial resolution and signal strength due to number of frames taken per second.
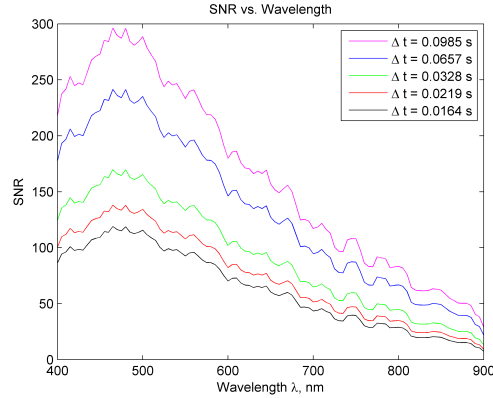

Fig. 9: SNR vs. exposure time, clearly showing increase in SNR as exposure time becomes longer.
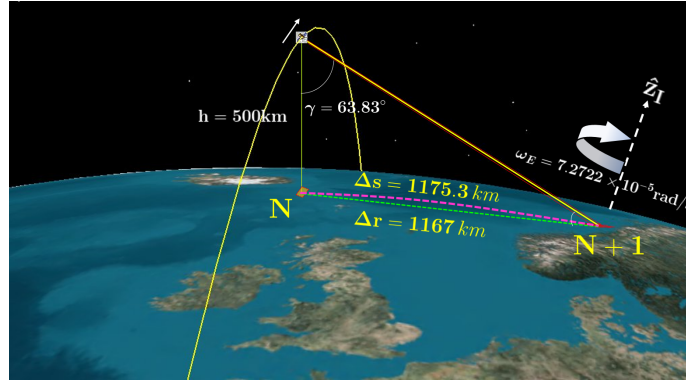
E. Viewing Angles

Fig. 10: `SmallSat` at $h = 500$ km in two consecutive passes with ≈ 96 minutes period, where $N + 1$ pass shows the target area (same ground point) has moved approximately 1175 km at latitude of 63.11°, resulting a required $\Delta \gamma \approx 64°$ from Nadir in cross-track direction. Now also spatial resolution has worsened.

Another requirement for the slewing motion is due to Earth's rotation, meaning that the spacecraft not only has to slew along-track but also in the cross-track direction given that the target area will move westwards in next pass. Two cases are to be considered:

- Figure 10 shows the example of the nominal pass where `SmallSat` at $h = 500$ km flies directly over the 50 km long target area, then needing to slew in the cross-track direction from Nadir, it can be shown that for the next pass after 96 min, the `SmallSat` would have to point to $\gamma \approx 64°$ due to the target that has moved 1175 km westwards.
- If the nominal `SmallSat` pass is right in the middle of the target in first and second pass then `SmallSat` would have to point to $\gamma \approx 45°$ wrt. Nadir due to the target having moved 588 km westwards.

Both the cases can be ameliorated based on altitude selection and independent camera pointing. However, spatial resolution will also worsen, since along-track spatial resolutions are expressed in terms of slant range ($r > h$).

$$\delta x = \frac{rw}{f_0} \tag{10}$$

and cross-track resolution is

$$\Delta y = \frac{rz}{f_0 N_p} \tag{11}$$

and solid angle of sensor is

$$\Omega_{\text{aperture}} = \frac{\pi(L_0/2)^2}{r^2} \tag{12}$$

where $r = h/\cos\gamma$ is the slant range and increases with larger viewing angles hence ground pixels become much larger and resolution of the target worsens. For $\gamma = 65°$, then $r = 1140.6$ km, $\delta x = 570.3$ m, $\Delta y = 118.3$ m and $\Omega_{\text{aperture}} = 9.43 \times 10^{-17}$.

Figure 11 shows how viewing angles affect SNR based on exposure time $\Delta t = 0.0328$ s. The water-leaving radiance now adheres to the phase function (assuming the water radiance is scattered by Lambertian BRDF) i.e.,

$$p(\gamma) = \frac{2}{3\pi^2}\left(\sin\gamma + (\pi - \gamma)\cos\gamma\right) \tag{13}$$

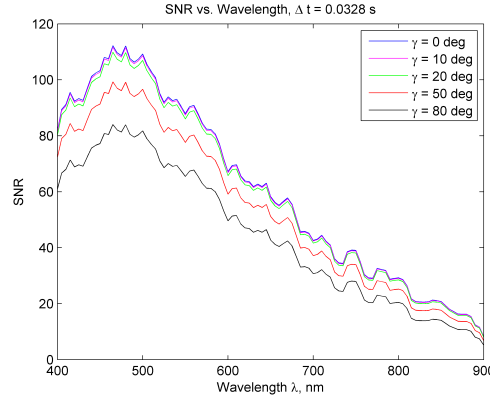Ideally, the water-leaving radiances may be simulated in MODTRAN at different viewing angles.

Fig. 11: SNR vs. viewing angles (with BRDF). For $\gamma = 80°$, then $r = 2879.4$ km, $\delta x = 1439.7$ m, $\Delta y = 298.7$m and $\Omega_{\text{aperture}} = 1.4802 \times 10^{-17}$.

F. Saturation

One way to avoid green saturation is to use an amethyst filter (e.g. http://www.koppglass.com/filter-catalog/purple-filter-glass.php) having a transmission curve that suppresses the green. Of course green signal is thrown away but at least can potentially improvement is made on the relative blue and red SNR while avoiding saturating the detector, which will likely render the whole frame indistinguishable; at best is to decimate the green part of the hypercube.

G. Stray Light

Stray light within the spectrograph may dominate the "noise" in the SNR problem. Any photon that does not reach the theoretically perfect place on the photodetector; that is the right row of color and the right column of cross-track location is called stray light. Sources include scattering/refraction from scratch and dig, stria, or cement flaws in the optics, monochromatic (Zernike) aberrations, chromatic aberration, polarization sensitivity, and non-ideal diffraction grating effects including scattering from ruling flaws, low diffraction efficiency (e.g. related to where the un-diffracted light goes), and poor order blocking filter performance. Characterization and correction schemes are given in [1].

III. ATMOSPHERIC CORRECTION

Aerosols, gases, humidity, bubbles etc. distort the spectral response for a HSI. Figure 6 shows this effect, where 85-95 % of photons (depending on wavelength) are coming directly from the atmosphere. Since NIR is absorbed by the atmosphere (and water) more than VIS, many atmospheric corrections are employed using NIR [2, 3].

The advantages and challenges with HSI coastal observations in space are discussed briefly in [4]. The water-leaving radiance generally only accounts for around 10-15 % of the signal that may be observed in space, with the

rest of the signal being corrupted by atmospheric and surface/landscape effects, especially for Case 2 waters being mostly coastal waters. It is noted that turbid waters and strong-absorbing aerosols occur in coastal waters which may bring challenges to remote sensing where NIR is necessary for these type of corrections. 700-800 nm may be used to discriminate clouds and land from the open ocean, as well as to map surface vegetation [4] such as on Coastal Zone Color Scanner (CZCS), launched by NASA in 1978.

Usage of HSI for high-sediment-loads observations (in VIS-NIR) is investigated by [5]. Spectral coverage to the shortwave-infrared (SWIR) region is useful for the estimation of suspended particulate matter (SPM) concentrations and for the correction of atmospheric contributions for remote sensing of coastal/in-land turbid waters. [6] also concludes with the necessity with NIR bands for proper atmospheric corrections, even for high Chl-a concentrations.

Hyperspectral Imager for the Coastal Ocean (HICO), mounted on ISS and retired in 2014, leveraged data to estimate Chl-a concentration in coastal waters, and was a successor to MEdium Resolution Imaging Spectrometer (MERIS). A further note on this is that it is common knowledge that MERIS superseded MODerate resolution Imaging Spectroradiometer (MODIS) given its band at 708 nm for estimating low-moderate Chl-a concentrations in turbid waters. HICO was a push broom sensor that captured data in the wavelength range 350-1080 nm, with a spectral resolution of 5.73 nm and GSD $\approx$ 90m. [7] presents the radiometric processing results and limitations using red-NIR models, as well as suggestions for future applications of spaceborne HSI in coastal waters. Again, high turbidity renders conventional blue-green algorithms unreliable for estimating Chl-a concentrations. To combat the optical complexity in such cloudy waters, algorithms for red and NIR regions of the spectrum have been recently developed and successfully validated for estimating Chl-a concentration in inland and coastal waters. HICO had problems with the red-NIR spectral range of 700-1080 nm due to contamination by diffracted second-order light in the wavelength range of 350-540 nm, from lack of an optical filter that would block out this second-order light. However there are empirical methods to alleviate this successfully [8], and by optical design [9]. The radiometric instability issue should be investigated further including the ability for onboard calibration (latter not possible for HICO). The visible light (400-700 nm) penetrates the water and provides information on water properties and bottom reflectance, and shortwave infrared radiation (700-900 nanometers) is used to correct for atmospheric aerosols and surface reflectance [2].

Hyperion, which was launched in 2000, has been used for coastal water studies. However, its SNR (50:1) was very low [10], and the sensor was unreliable in quantitatively estimating water quality parameters due to problems such as radiometric instability [11]. HICO, on the other hand has high SNR (200:1) over the visible wavelengths [2]. Even SNR of $> 200 : 1$ is achieved for NIR wavelengths, assuming 5 % albedo.

Spatial ground resolution of 100 m is recommended in order to characterize ocean coastal waters, and even higher resolution is required for high biodiversity of phytoplankton in certain coastal and inland waters [4]. LandSat for instance, "accidentally" proved useful for ocean color due to the high resolution, even though the application was not intended. [4] provides an overview of current and previous HSI flights as well as challenges.

Furthermore, [12] presents results using NIR bands for Chl-a concentration estimation from HICO and states that, apart from visible wavelengths for direct chlorophyll observations, shortwave infrared radiation (700-900 nm) is used to correct for atmospheric aerosols and surface reflectance [2]. It is especially important with these corrections for the retrieval of low-to-moderate Chl-a concentration.

Radiometric resolution datasheets on Sentinel-3 Ocean and Land Colour Instrument (OLCI) exist where the application of each spectral band is indicated[3]. OLCI is a push-broom imaging spectrometer with five cameras, where mitigation of sun-glint contamination is done by tilting cameras in westerly direction. Other specs for the OLCI are: swath width of 1270 km, spectral range of 400-1020 nm and spatial sampling of 300 m. From the datasheet it is evident what functionality each of the NIR bands have: 778.75 nm for atmospheric and aerosol corrections; 865 nm for atmospheric and aerosol corrections, clouds, pixel co-registration; 885 nm for water vapour absorption reference band and is the common reference band with SLSTR instrument, also used for vegetation monitoring; 900 nm for water vapour absorption/vegetation monitoring (max. reflectance).

See Fig. 12 for an overview of usage of the spectral bands in satellite missions.

---

[3]https://sentinel.esa.int/web/sentinel/user-guides/sentinel-3-olci/resolutions/radiometric
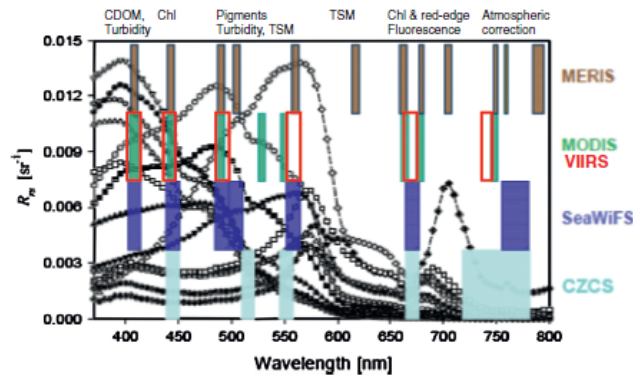
Fig. 12: Satellite missions with Multi-spectral Imagers and utilization of each spectral bands [3]

Several other techniques are also envisaged to be investigated in contrast to the standard techniques in atmospheric correction. These involve using analytical algorithms based on the derivatives of the radiative transfer equation, termed as the derivative ratio algorithm [13]. A spectral shape algorithm that uses derivatives has been applied to Medium Resolution Imaging Spectrometer (MERIS) imagery that has detected cyanobacterial blooms, with extensive examples in Lake Erie [14]. The detection algorithm uses an approximation of the second derivative as a measure of spectral shape around the 681 nm band and has proven that these algorithms prove successful results without compromising the systematic noise in SNR.

IV. CAMERA CALIBRATION

Suggestions on calibration for HSI testbed to image the following (in order of priority):

1) Monochromatic light source (e.g. 550 nm), see if we can get the spectral response matching apriori knowledge of spectral band. Determine if sensor output spectral response is shifted from nominal. May use spectral photometer.
2) Blue sky and characterize the spectral response as above in 1.
3) Black body source of light. Characterize spatial vs. spectral response. Characterize Quantization Efficiency at different wavelengths.
4) Diffuse source of light (e.g. water) - even illumination (not focused images)
5) Closing the camera cap to characterize dark noise, bias and read-out noise with different in exposure times based on camera specifications.
6) Any source of light (clean room) and subtract the noise to see signal response.

It is important to characterize Quantization Efficiency across wavelengths, edges of spectral range (400-900 nm) have lower quantization efficiency (vignetting). Additional noise comes from microbubbles (Rayleigh scattering) and also needs to be characterized (microbubbles most likely have noise described as random or by Brown distortion model).

One option is to take several images of a track and average those multiple images to estimate the noise in the camera and scene. Determine PSNR for image reconstruction, also SNR to characterize image before and after reconstruction.

V. HYPERSPECTRAL INSTRUMENT DESIGNS

Table V offers spectrometer designs that are different but may achieve same goals as the HSI version 4 and 5.

TABLE V: Spectrometer designs

Type	Description
PRISM "Dyson" [15]	Considered the "best" dark target pushbroom hyperspectral prototype to consider, combining low f-number, low internal scattering, and low monochromatic and chromatic aberrations to maximize SNR over dark targets.
Offner [16]	Three-concentric-mirror (Offner) configuration. The approach presented allows for the rapid design of this class of system.
CHAI V-640 [4]	Commonly used airborne sensor for validation campaigns for remote sensing (satellite hyperspectral imagery)
NovaSol [5]	Airborne hyperspectral design but possibly at larger form factor

REFERENCES

[1] Y. Zonga, S. W. Browna, G. Meisterb, R. A. Barnesc, and K. R. Lykke. Characterization and correction of stray light in optical instruments. *Proc. of SPIE*, 6744, 2007. doi: http://dx.doi.org/10.1117/12.737315. 9

[2] M. R. Corson and C. O. Davis. A New View of Coastal Oceans From the Space Station. *EOS, Transactions, American Geophysical Union*, 92:161–168, 2011. doi: 10.1029/2011EO190001. 9, 10

[3] David Blondeau-Patissier, James F.R. Gower, Arnold G. Dekker, Stuart R. Phinn, and Vittorio E. Brando. A review of ocean color remote sensing methods and statistical techniques for the detection, mapping and analysis of phytoplankton blooms in coastal and open oceans. *Progress in Oceanography*, 123:123–144, 2014. doi: https://doi.org/10.1016/j.pocean.2013.12.008. 9, 11

[4] Simon Emberton, Lars Chittka, Andrea Cavallaro, and Menghua Wang. Sensor Capability and Atmospheric Correction in Ocean Colour Remote Sensing. *Remote Sensing*, 8, 2016. doi: 10.3390/rs8010001. 9, 10

[5] Z. Lee, S. Shang, G. Lin, J. Chen, and D. Doxaran. On the modeling of hyperspectral remote-sensing reflectance of high-sediment-load waters in the visible to shortwave-infrared domain. *Applied Optics*, 55: 1738–1750, 2016. doi: https://doi.org/10.1364/AO.55.001738. 10

[6] D. A. Siegel, M. Wang, S. Maritorena, and W. Robinson. Atmospheric Correction of Satellite Ocean Color Imagery: The Black Pixel Assumption. *Applied Optics*, 39, 2000. doi: https://doi.org/10.1364/AO.39.003582. 10

[7] Wesley Moses, Anatoly Gitelson, Sergey Berdnikov, Jeffrey Bowles, Vasiliy Povazhnyi, Vladislav Saprygin, Ellen Wagner, and Karen Patterson. HICO-Based NIRRed Models for Estimating Chlorophyll-a Concentration in Productive Coastal Waters. *IEEE Geoscience and Remote Sensing Letters*, 2013. doi: 10.1109/LGRS.2013. 2287458. 10

[8] R-R. Li, R. Lucke, D. Korwan, and B-C. Gao. A technique for removing second-order light effects from hyperspectral imaging data. *IEEE Trans. Geosci. Remote Sens.*, 50:824–830, 2012. doi: 10.1109/TGRS.2011. 2163161. 10

[9] F. Sigernes, M. Syrjasuo, R. Storvold, J. Fortuna, M. Grøtte, and T. A. Johansen. A 3D printed hyperspectral imager. Technical report, University Center in Svalbard, 2017. 10

[10] C. Hu, L. Feng, Z. Lee, C. O. Davis, A. Mannino, C. R. McClain, and B. A. Franz. Dynamic range and sensitivity requirements of satellite ocean color sensors: Learning from the past. *Applied Optics*, 51:60456062, 2012. doi: https://doi.org/10.1364/AO.51.006045. 10

[11] National Research Council. Earth science and applications from space: National imperatives for the next decade and beyond. Washington, DC, USA: The National Academic Press, 2007. 10

[12] A. Gitelson, B. C. Gao, R-R. Li, S. Berdnikov, and V. Saprygin. Estimation of chlorophyll-a concentration in productive turbid waters using a Hyperspectral Imager for the Coastal Oceanthe Azov Sea case study. *Environmental Research Letters*, 6, 2011. doi: 10.1088/1748-9326/6/2/024023. 10

[13] William D. Philpot. Atmospheric Effects in Remote Sensing. *IEEE Transactions on Geoscience and Remote Sensing*, 29(3), 1991. 11

[14] T. T. Wynne, R. P. Stumpf, and T. O. Briggs. Comparing MODIS and MERIS spectral shapes for cyanobacterial bloom detection. *International Journal of Remote Sensing*, 2013. doi: http://dx.doi.org/10.1080/01431161. 2013.804228. 11

[15] P. Mouroulis, B. V. Gorp, R. O. Green, H. Dierssen, D. W. Wilson, M. Eastwood, J. Boardman, B. Gao, D. Cohen, B. Franklin, F. Loya, S. Lundeen, A. Mazer, I. McCubbin, D. Randall, B. Richardson, J. I. Rodriguez, C. Sarture, E. Urquiza, R. Vargas, V. White, and K. Yee. The Portable Remote Imaging Spectrometer (PRISM)

coastal ocean sensor: design, characteristics and first flight results. *Applied Optics*, 53(7):1363–1380, 2014. doi: https://doi.org/10.1364/AO.53.001363. 12

[16] X. Prieto-Blanco, C. Montero-Orille, B. Couce, and R. de la Fuente. Analytical design of an Offner imaging spectrometer. *Optics Express*, 14(20), 2006. doi: https://doi.org/10.1364/OE.14.009156. 12